How to cite: *Angew. Chem. Int. Ed.* **2021**, *60*, 19041 – 19046
International Edition: doi.org/10.1002/anie.202106128
German Edition: doi.org/10.1002/ange.202106128

Label-Free Imaging

Nanoscale Chemical Imaging of Supported Lipid Monolayers using Tip-Enhanced Raman Spectroscopy

Yashashwa Pandey, Naresh Kumar, Guillaume Goubert, and Renato Zenobi**

Abstract: *Visualizing the molecular organization of lipid membranes is essential to comprehend their biological functions. However, current analytical techniques fail to provide a non-destructive and label-free characterization of lipid films under ambient conditions at nanometer length scales. In this work, we demonstrate the capability of tip-enhanced Raman spectroscopy (TERS) to probe the molecular organization of supported DPPC monolayers on Au (111), prepared using the Langmuir–Blodgett (LB) technique. High-quality TERS spectra were obtained, that permitted a direct correlation of the topography of the lipid monolayer with its TERS image for the first time. Furthermore, hyperspectral TERS imaging revealed the presence of nanometer-sized holes within a continuous DPPC monolayer structure. This shows that a homogeneously transferred LB monolayer is heterogeneous at the nanoscale. Finally, the high sensitivity and spatial resolution down to 20 nm of TERS imaging enabled reproducible, hyperspectral visualization of molecular disorder in the DPPC monolayers, demonstrating that TERS is a promising nanoanalytical tool to investigate the molecular organization of lipid membranes.*

Supported lipid monolayers are an excellent system for studying a range of molecular phenomena in the field of membrane biophysics[1] such as protein-membrane interaction,[2] drug-membrane interaction[3] and enzymatic reactions in two dimensions.[4] Structured Langmuir–Blodgett (LB) lipid monolayers are also promising model systems for tribological studies such as wetting and adsorption in coatings.[1,5] Successful biological, optical, electronic, and sensing applications of LB films[6] are underpinned by accurate chemical and structural characterization at the nanometer scale. However, visualizing the molecular structure of lipid membranes at the nanoscale remains highly challenging because of the lack of a sensitive, non-invasive, and label-free nanoanalytical tool that can be used under ambient conditions. For example, conventional optical spectroscopy techniques such as Raman, infra-red (IR) and fluorescence spectroscopies fail to achieve this goal due to the optical diffraction limit.[7] Therefore, confocal optical microscopy cannot typically provide spatially resolved information about phase-separated domains inside lipid membranes that are less than 200 nm in size.[8] Super-resolution fluorescence microscopy (SRFM) can be used to visualize coexisting molecular domains in model membranes as well as cell membranes at the nanoscale.[9] However, SRFM is limited by the essential requirement of extrinsic fluorescent probes with an affinity for particular lipid phases. These fluorescent probes can perturb phase behavior of lipid mixtures and have been shown to reduce the amount of liquid condensed (LC) phase by 10–20%, decrease film stability, increase equilibration time and influence the area, shape, and interconnectivity of phase-separated lipid domains.[10] Similarly, scanning probe microscopy (SPM) can provide topography information with molecular resolution; however, the chemical information is inadequate for detailed molecular visualization of lipid membranes.[11]

Tip-enhanced Raman spectroscopy (TERS) has emerged as a powerful tool for non-destructive and label-free correlative topographical and chemical imaging at the nanoscale, and overcomes the limitations of confocal optical microscopy, SRFM, and SPM.[12] In TERS, a metallic SPM probe placed in the focal spot of an excitation laser confines and enhances the electromagnetic field in the nanoscopic volume at the probe apex *via* a combination of localized surface plasmon resonance (LSPR) and lightening rod effect. Therefore, TERS combines the high spatial resolution of SPM with the chemical sensitivity of surface-enhanced Raman spectroscopy providing molecular imaging at the nanometer length scales. With a high spatial resolution and sensitivity, TERS has been successfully used to investigate biological samples including cells,[13] proteins,[14] and biomembranes.[15] However, the reported TERS measurements sometimes required deuterium labelling and often suffered from poor spectral and imaging reproducibility, making interpretation difficult.

In this work, we use scanning tunneling microscopy (STM)-TERS imaging to investigate the molecular organization of a dipalmitoylphosphatidylcholine (DPPC) monolayer on Au (111) prepared using LB technique. DPPC monolayers are an important constituent of pulmonary surfactants, which modulate surface tension of the lungs, stabilize alveolar collapse during expiration and minimize work required to expand the alveoli during inhalation.[16] On the alveolar

[*] Y. Pandey, Dr. N. Kumar, Dr. G. Goubert, Prof. R. Zenobi
Department of Chemistry and Applied Biosciences, ETH Zurich
Vladimir-Prelog-Weg 1–5/10, 8093 Zürich (Switzerland)
E-mail: naresh.kumar@org.chem.ethz.ch
zenobi@org.chem.ethz.ch
Dr. G. Goubert
Current address: Department of Chemistry, Université du Québec à Montréal
Montreal, Québec, H2X 2J6 (Canada)
Supporting information and the ORCID identification number(s) for the author(s) of this article can be found under: https://doi.org/10.1002/anie.202106128.

surface, DPPC can assemble in either LC or liquid expanded (LE) phases. The phase transition from LC to LE and vice versa in DPPC monolayers enables modulation of the surface pressure, believed to maintain low surface tension during breathing.[16b,c,17] Therefore, understanding molecular organization into distinctly different phases is key to fully comprehend the biological functions of DPPC monolayers.[18]

Herein, we demonstrate that TERS is an effective analytical tool for nanoscale chemical characterization of a DPPC monolayer supported on Au (111), providing molecular insights that cannot be obtained using conventional analytical techniques. Reproducible TERS spectra with a significantly better signal-to-noise ratio than reported to date were obtained *via* careful optimization of DPPC monolayer preparation, plasmonically active and robust TERS probes, and experimental protocols. The high-quality TERS spectral data allowed a direct correlation of STM topography and TERS images of a DPPC monolayer for the first time. TERS imaging also revealed the presence of nanoscopic holes within the continuous DPPC monolayers,[19] which have not been spectroscopically observed before. Finally, the high sensitivity and spatial resolution of TERS allowed reproducible hyperspectral visualization of molecular disorder within DPPC monolayers. These results demonstrate that TERS is a promising tool to investigate the molecular organization of lipid membranes at nanometer length scales in a non-destructive and label-free fashion.

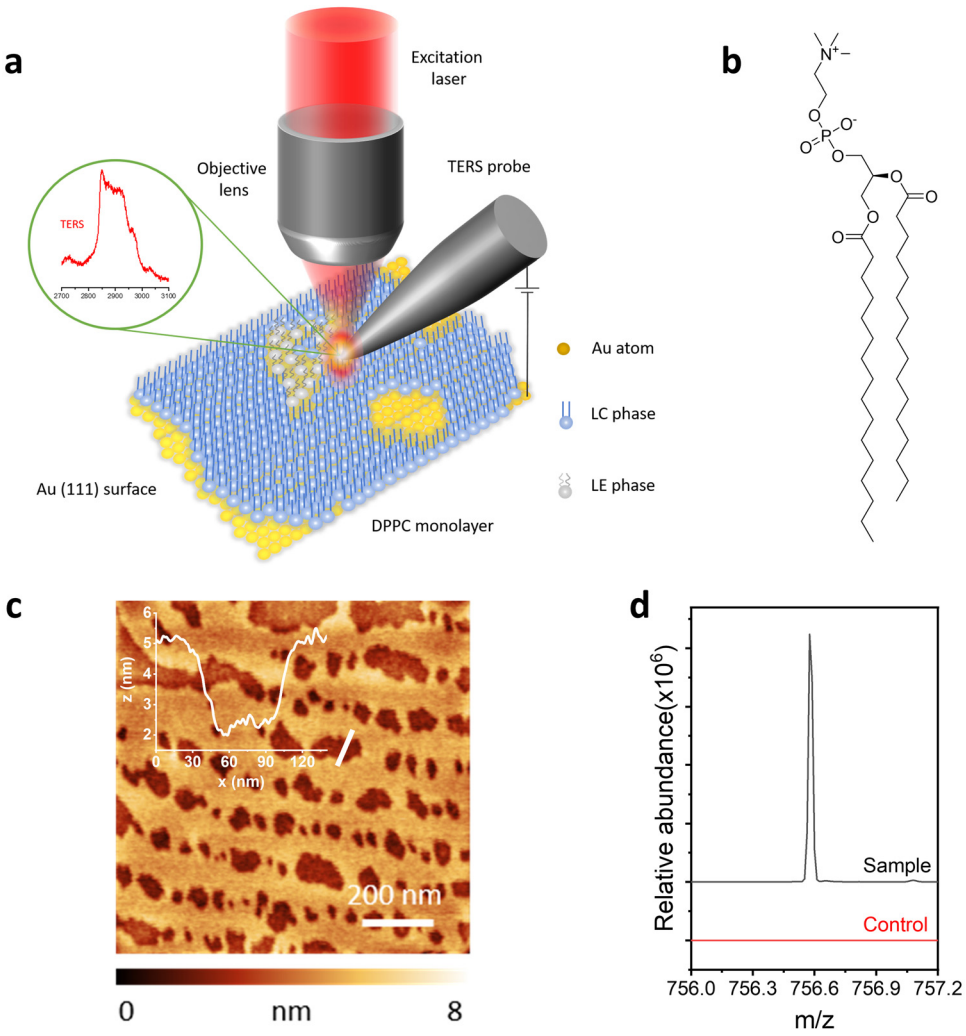

Figure 1. (a) Experimental set-up used for TERS imaging of supported DPPC monolayers in this work. (b) Chemical structure of a DPPC molecule. (c) AFM topography image of DPPC monolayer transferred onto a Au (111) surface using LB technique. Inset shows a height profile along the white line. (d) Nano-ESI mass spectra of a Au surface with (black) and without (red) DPPC monolayer.

A schematic diagram of the STM-TERS set-up used in this work is shown in Figure 1 a. Further experimental details are presented in the Supplementary Information. Figure 1 b shows the chemical structure of a DPPC molecule. An AFM topography image of a DPPC monolayer transferred onto a Au (111) surface using LB technique at 20 mN m^{-1} is shown in Figure 1 c. The transfer isotherm of the DPPC monolayer is presented in Figure S1. The topography image shows several regions of discontinuity in the DPPC monolayer. The height difference between the DPPC layer and the Au (111) substrate is 2.74 ± 0.03 nm (see inset), which correlates very well with the 2.8 nm height of a DPPC molecule and confirms the monolayer nature of the transferred film[20] (see Figure S2 for further analysis of the topography image). The presence of DPPC in the monolayer transferred onto Au was further confirmed using nano-electrospray ionization mass spectrometry measurements presented in Figure 1 d, where a [DPPC + Na^+] peak at $m/z = 756.6$ is clearly visible in the mass spectrum of a sample collected from the DPPC monolayer-covered Au surface, whilst it is absent in the control sample.

Before carrying out a detailed investigation of the DPPC monolayer, we first checked the sensitivity and reproducibility of our TERS measurements. No bands were observed in the far-field Raman spectrum of the DPPC monolayer due to the low sensitivity of confocal Raman measurements, as shown in Figure S3. However, the TERS spectrum of a DPPC monolayer showed clear Raman bands, confirming a strong plasmonic enhancement of Raman signals in the near field (Figure S3). Interestingly, only Raman bands in the C-H stretching region (2800–3100 cm^{-1}) were enhanced in the

TERS spectra, whereas no bands were observed in the fingerprint region. This is possibly due to the surface organization of the lipid layer with the alkyls pointing out of the surface plane. In this case, C-H stretching modes will dominate the spectra while contribution of other bands is suppressed. Furthermore, the relatively low intensity of the Raman peaks in the fingerprint region compared to the C-H stretch region[21] could also contribute to the non-visualization of Raman bands in the fingerprint region. To check reproducibility, three TERS images of the C-H stretching band were measured consecutively in a region of DPPC monolayer as shown in Figure S4. The TERS images showed similar features with no degradation of the signal, demonstrating the stability of our TERS set-up for reproducible TERS imaging.

Figure 2a shows a STM topography image of a patch of DPPC monolayer on Au (111) measured simultaneously with the TERS image. TERS image of the C-H stretching intensity is shown in Figure 2b, which matches very well with the corresponding topography image. This is the first direct correlation of a DPPC monolayer topography with the TERS image of the same region. The TERS image reveals several novel features that are not visible in the topography image in Figure 2a. For example, the TERS signal intensity varies significantly in different parts of the monolayer and disappears completely at certain locations. This indicates a non-uniform packing order in the transferred DPPC monolayer. TERS spectra measured from five high-intensity pixels marked with red crosses and five low-intensity pixels marked with white crosses in Figure 2b are plotted in Figure 2c. A clear TERS signal is observed from the DPPC monolayer at locations of high signal intensity. However, the signal disappears completely at the locations of low signal intensity, indicating the presence of holes within the DPPC monolayer. This implies that at the nanoscale, the DPPC monolayer is not a continuous film and such discontinuities are present throughout the transferred monolayer. Furthermore, from the absence of Raman bands at different locations inside the DPPC monolayer, size of the holes is estimated to be 40–120 nm. This is the first direct hyperspectral visualization of such nanoscale features inside a supported lipid monolayer. Interestingly, these nanoscopic features are not visible in the STM image. This may be due to the relatively large step size (40 nm) of the STM-TERS image and the relatively large diameter (*ca.* 50 nm) of the TERS probe apex. In STM imaging, the acquired topographical image is a con-

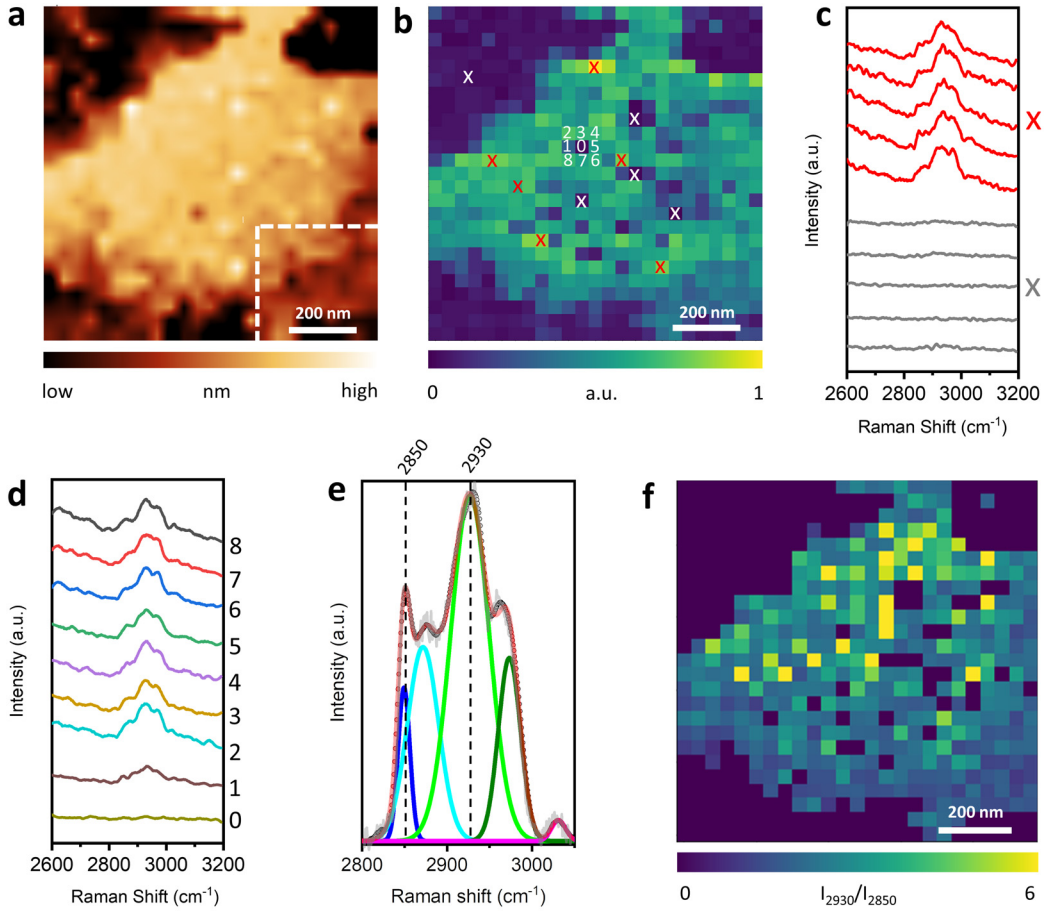

Figure 2. (a) STM topography image of a DPPC monolayer region on Au (111). (b) TERS image of the C-H stretching (2800–3000 cm^{-1}) intensity measured in the area shown in (a). Integration time: 2 s. Step size: 40 nm. (c) TERS spectra measured at the locations of high signal intensity marked as "red x" and locations of low signal intensity marked as "white x" in (b). (d) TERS spectra of the pixels marked as 0–8 in (b). (e) Average TERS spectrum of the TERS image in (b) fitted with Gaussian curves. (f) TERS image of the I_{2930}/I_{2850} ratio.

volution of the probe shape, apex diameter, and sample topography. This can broaden the topographic features and reduce corrugation amplitudes, especially in samples with relatively large height differences,[22] which is the case for our DPPC monolayer sample, where the height difference is 2.7 nm (see inset of Figure 1c and Figure S2). However, the highly localized nature of the TERS near-field renders these features clearly visible in the TERS image.[23]

To determine the spatial resolution of the TERS image, TERS spectra from locations marked 0–8 in Figure 2b are plotted in Figure 2d. Location 0 represents the spectrum measured at a hole in the DPPC monolayer, whereas locations 1 through 8 represent the TERS spectra measured within one step (40 nm) of the hole. It can be clearly seen that in contrast to the neighboring pixels (1–8), no TERS signal is observed at location 0. This shows that TERS imaging can successfully resolve sample features of size 40 nm. This is $\approx 14\times$ higher than the 551 nm diffraction-limited optical resolution of our TERS system calculated using $0.61\lambda/NA$, where λ is the wavelength of the excitation laser (633 nm) and NA is the numerical aperture (0.7) of the objective lens.

Assignment of bands in the DPPC TERS spectrum is presented in Table S1. The Raman band at 2850 cm^{-1} represents the methylene symmetric stretch (d^+) of the lipid chains,[24] whereas the Raman band at 2930 cm^{-1} arises from the Fermi resonance associated with the terminal methyl symmetric stretch (r^+_{FR}) and the C-H bending mode.[24] The ratio of these two bands (I_{2930}/I_{2850}) is a measure of the intermolecular chain coupling in the DPPC monolayer. A high I_{2930}/I_{2850} ratio signifies an increased vibrational and rotational freedom of movement of the terminal methyl group compared to the methylene chain of the DPPC molecules indicating a greater disorder within the monolayer.[24b,25] Therefore, we used the I_{2930}/I_{2850} ratio to infer nanoscale packing order of the lipid monolayer. Using the intensity ratio of the two TERS bands has the additional advantage of eliminating the effects of local and temporal fluctuations in TERS signal enhancement, which provides a more accurate visualization of the molecular arrangement. I_{2930}/I_{2850} ratio was determined from deconvolution of the TERS bands using Gaussian fitting of the C-H stretching region as shown in Figure 2e. A TERS image of the I_{2930}/I_{2850} ratio is presented in Figure 2f, where a significant heterogeneity in the packing order is observed across the DPPC monolayer. Figure S5 shows analysis of the signal-to-noise in the I_{2930}/I_{2850} ratio image confirming that the signal variation comes from the sample and not from the instrumental noise. A higher I_{2930}/I_{2850} ratio is observed around the holes, signifying a relatively higher level of disorder. This indicates that the creation of holes leads to a disruption of molecular packing in the lipid monolayer. Furthermore, there is an increase in lipid order (decrease in I_{2930}/I_{2850} ratio) from the top right to the bottom left of the DPPC monolayer patch, which signifies spatial variation in the relative orientation of the lipid monolayer. See Figures S6 and S7 for further discussion about the statistical significance of these results.

TERS imaging of the region marked in white in Figure 2a is presented in Figure 3. Similar results are obtained in the zoomed-in TERS image in Figure 3b, which showed a significant variation in the TERS signal intensity across the DPPC monolayer and absence of TERS signals at certain locations (Figure 3c) indicating the presence of holes. A notable heterogeneity in the lipid packing order was observed in the I_{2930}/I_{2850} ratio image in Figure 3d, which showed distinct areas of higher and lower disorder. These results further demonstrate the reproducibility of TERS measurements on supported DPPC monolayers on Au (111). High-resolution TERS imaging in Figure 2 and Figure 3 show that in the case of a lipid membrane transferred at high surface pressure, a disordering of the lipid molecules could take place at the nanometer scale, leading to segregation of the lipid monolayer into areas of discontinuity as well as regions of higher and lower disorder.

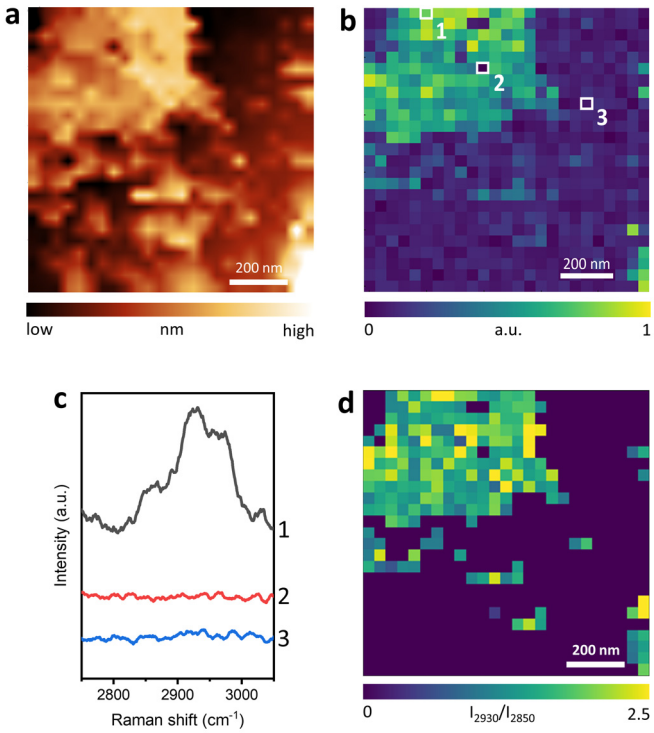

Figure 3. (a) STM topography image of the DPPC monolayer region marked in white in Figure 2a. (b) TERS image of the C-H stretching intensity measured in the area shown in (a). Integration time: 2 s. Step size: 40 nm. (c) TERS spectra measured at locations 1–3 marked in (b). (d) TERS image of the I_{2930}/I_{2850} ratio.

Finally, we investigated organization of a DPPC monolayer in a region of Au (111) that contains several terraces and steps. A TERS image of the C-H stretching intensity in such a region is shown in Figure 4a and the corresponding STM topography image is presented in Figure S8. In the TERS image, different terraces of the Au (111) surface are clearly resolved together with the terrace steps, which appear as diagonal lines in the image with zero signal intensity. Several regions of the terrace steps show zero TERS signal intensity at individual pixels indicating a spatial resolution of 20 nm. The absence of the TERS signal at the steps indicates breakage of the DPPC monolayer. Further examination of the TERS image for molecular packing order gives some interesting insights. The non-uniform TERS signal intensity

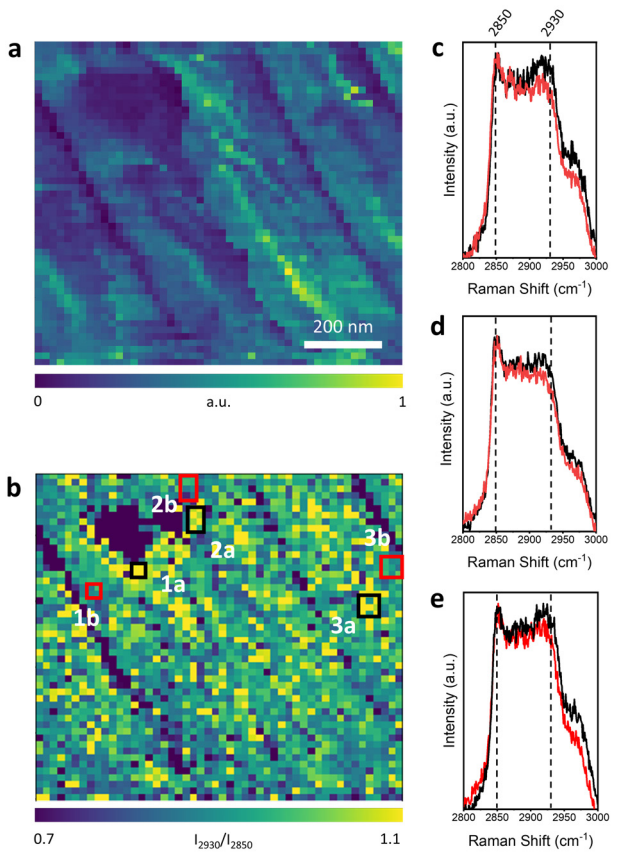

Figure 4. (a) TERS image of the C-H stretching intensity in a sample region containing several terraces. Integration time: 2 s. Step size: 20 nm. (b) TERS image of the I_{2930}/I_{2850} ratio. (c), (d), (e), Average TERS spectra measured at the regions of high (1 a, 2 a and 3 a, black squares) and low (1 b, 2 b and 3 b, red squares) I_{2930}/I_{2850} ratio marked in (b).

across the terraces suggests differences in the molecular arrangement of DPPC molecules. To visualize this more clearly, a TERS image of the I_{2930}/I_{2850} ratio is presented in Figure 4 b. In this image, regions of higher molecular disorder (high I_{2930}/I_{2850} ratio) can be clearly distinguished from regions of lower molecular disorder. Figures 4 c, 4 d, and 4 e show averaged TERS spectra from different areas of high (black squares) and low (red squares) signal intensity marked as 1 a and 1 b (1600 nm^2), 2 a and 2 b (2400 nm^2), and 3 a and 3 b (3600 nm^2) in Figure 4 b. Note that even though regions "a" (black curve) and "b" (red curve) are on the same terrace, their spectral shape is different. Regions "a" (black curves) have a slightly higher I_{2930}/I_{2850} ratio compared to regions "b" (red curves), which clearly indicates a relatively different molecular arrangement in different areas of the same Au (111) terrace. See Figures S9 and S10 for further analysis of the signal-to-noise and statistical significance of these results. This study establishes that even a homogenously transferred DPPC monolayer on a Au (111) surface could be heterogenous at the nanoscale.

In summary, we have demonstrated non-destructive and label-free hyperspectral chemical imaging of a supported lipid monolayer with 20 nm resolution using TERS for the first time. High signal-to-noise ratio spectra enabled reproducible TERS imaging of DPPC monolayers on a Au (111) surface and a direct correlation of the TERS and topography images. TERS imaging provided spectroscopic visualization of nanoscale structural features such as holes as well as local variations in the lipid packing order in the transferred DPPC film. High-resolution TERS imaging even revealed differences in the lipid molecular arrangement on the same single crystal terrace, which has not been observed before. These results unequivocally demonstrate that TERS is a reliable tool for the nanoscale structural and chemical characterization of the molecular organization in supported lipid monolayer systems. This work opens the door for direct, non-destructive, and label-free molecular visualization of more complex biological membranes at the nanoscale using TERS.

Acknowledgements

We thank Dr. Zhenfeng Cai (ETH Zurich) for help with the preparation of Au (111) substrates, Jonas Metternich and Qinlei Liu (ETH Zurich) for mass spectrometry measurements and and Dr. Amit Kumar Sachan (ETH Zurich) for LB film training. The authors acknowledge funding from the European Union through ERC grant no. 741431 (2D Nano-Spec). The original data used in this publication are made available in a curated data archive at ETH Zurich (https://www.research-collection.ethz.ch) under the DOI 10.3929/ethz-b-000491241.

Conflict of Interest

The authors declare no conflict of interest.

Keywords: DPPC · Langmuir–Blodgett films · monolayer · nanoscale chemical imaging · phospholipids · tip-enhanced Raman spectroscopy

[1] V. M. Kaganer, H. Mohwald, P. Dutta, *Rev. Mod. Phys.* **1999**, *71*, 779–819.
[2] H. Brockman, *Curr. Opin. Struct. Biol.* **1999**, *9*, 438–443.
[3] a) M. Lúcio, F. Bringezu, S. Reis, J. L. F. C. Lima, G. Brezesinski, *Langmuir* **2008**, *24*, 4132–4139; b) M. Broniatowski, M. Flasiński, P. Wydro, *J. Colloid Interface Sci.* **2012**, *381*, 116–124.
[4] S. Ransac, M. Ivanova, I. Panaiotov, R. Verger, in *Lipase and Phospholipase Protocols, Vol. 109* (Eds.: M. Doolittle, K. Reue), Humana Press, Totowa, **1999**, pp. 279–302.
[5] a) V. N. Bliznyuk, M. P. Everson, V. V. Tsukruk, *J. Tribol.* **1998**, *120*, 489–495; b) V. V. Tsukruk, V. N. Bliznyuk, J. Hazel, D. Visser, M. P. Everson, *Langmuir* **1996**, *12*, 4840–4849; c) M. Rojewska, M. Skrzypiec, K. Prochaska, *Chem. Phys. Lipids* **2019**, *221*, 158–166; d) M. I. Boyanov, J. Kmetko, T. Shibata, A. Datta, P. Dutta, B. A. Bunker, *J. Phys. Chem. B* **2003**, *107*, 9780–9788; e) D. Paiva, G. Brezesinski, M. D. C. Pereira, S. Rocha, *Langmuir* **2013**, *29*, 1920–1925.
[6] a) I. R. Girling, S. R. Jethwa, R. T. Stewart, J. D. Earls, G. H. Cross, N. A. Cade, P. V. Kolinsky, R. J. Jones, I. R. Peterson, *Thin Solid Films* **1988**, *160*, 355–362; b) A. S. Sizov, A. A. Trul, V. Chekusova, O. V. Borshchev, A. A. Vasiliev, E. V. Agina, S. A. Ponomarenko, *ACS Appl. Mater. Interfaces* **2018**, *10*, 43831–

43841; c) A. Tao, F. Kim, C. Hess, J. Goldberger, R. He, Y. Sun, Y. Xia, P. Yang, *Nano Lett.* **2003**, *3*, 1229 – 1233; d) G. G. Roberts, *Adv. Phys.* **1985**, *34*, 475 – 512.
[7] E. Abbe, *Arch. Mikrosk. Anat.* **1873**, *9*, 413 – 418.
[8] J. Korlach, P. Schwille, W. W. Webb, G. W. Feigenson, *Proc. Natl. Acad. Sci. USA* **1999**, *96*, 8461 – 8466.
[9] S. W. Hell, *Science* **2007**, *316*, 1153.
[10] a) S. L. Veatch, S. S. W. Leung, R. E. W. Hancock, J. L. Thewalt, *J. Phys. Chem. B* **2007**, *111*, 502 – 504; b) A. Cruz, L. Vázquez, M. Vélez, J. Pérez-Gil, *Langmuir* **2005**, *21*, 5349 – 5355.
[11] a) L. Eng, H. R. Hidber, L. Rosenthaler, U. Staufer, R. Wiesendanger, H. J. Güntherodt, L. Tamm, *J. Vac. Sci. Technol. A* **1988**, *6*, 358 – 359; b) J. Y. Fang, Z. H. Lu, L. Wang, Y. Wei, *Phys. Lett. A* **1992**, *166*, 373 – 376; c) C. W. Hollars, R. C. Dunn, *Biophys. J.* **1998**, *75*, 342 – 353; d) X. M. Yang, D. Xiao, S. J. Xiao, Y. Wei, *Appl. Phys. A* **1994**, *59*, 139 – 143.
[12] a) B.-S. Yeo, J. Stadler, T. Schmid, R. Zenobi, W. Zhang, *Chem. Phys. Lett.* **2009**, *472*, 1 – 13; b) N. Kumar, S. Mignuzzi, W. Su, D. Roy, *EPJ Tech. Instrum.* **2015**, *2*, 9; c) N. Kumar, B. M. Weckhuysen, A. J. Wain, A. J. Pollard, *Nat. Protoc.* **2019**, *14*, 1169 – 1193.
[13] a) N. Kumar, M. M. Drozdz, H. Jiang, D. M. Santos, D. J. Vaux, *Chem. Commun.* **2017**, *53*, 2451 – 2454; b) R. Böhme, M. Richter, D. Cialla, P. Rösch, V. Deckert, J. Popp, *J. Raman Spectrosc.* **2009**, *40*, 1452 – 1457.
[14] N. Kumar, in *Amino Acids, Peptides and Proteins, Vol. 43* (Eds.: M. Ryadnov, F. Hudecz), The Royal Society of Chemistry, Croydon, **2019**, pp. 127 – 153.
[15] a) L. Opilik, T. Bauer, T. Schmid, J. Stadler, R. Zenobi, *Phys. Chem. Chem. Phys.* **2011**, *13*, 9978 – 9981; b) A. Nakata, T. Nomoto, T. Toyota, M. Fujinami, *Anal. Sci.* **2013**, *29*, 865 – 869; c) R. Böhme, D. Cialla, M. Richter, P. Rösch, J. Popp, V. Deckert, *J. Biophotonics* **2010**, *3*, 455 – 461.
[16] a) B. Piknova, V. Schram, S. Hall, *Curr. Opin. Struct. Biol.* **2002**, *12*, 487 – 494; b) R. Wüstneck, J. Perez-Gil, N. Wüstneck, A. Cruz, V. B. Fainerman, U. Pison, *Adv. Colloid Interface Sci.* **2005**, *117*, 33 – 58; c) Y. Y. Zuo, R. A. W. Veldhuizen, A. W. Neumann, N. O. Petersen, F. Possmayer, *Biochim. Biophys. Acta Biomembr.* **2008**, *1778*, 1947 – 1977.
[17] a) L. K. Nielsen, T. Bjørnholm, O. G. Mouritsen, *Langmuir* **2007**, *23*, 11684 – 11692; b) Y. Y. Zuo, E. Keating, L. Zhao, S. M. Tadayyon, R. A. W. Veldhuizen, N. O. Petersen, F. Possmayer, *Biophys. J.* **2008**, *94*, 3549 – 3564.
[18] M. Stepanova, *Biophys. J.* **2009**, *96*, 4896 – 4905.
[19] a) A. Cruz, L. Vázquez, M. Vélez, J. Pérez-Gil, *Biophys. J.* **2004**, *86*, 308 – 320; b) R. Viswanathan, D. Schwartz, J. Garnaes, J. Zasadzinski, *Langmuir* **1992**, *8*, 1603 – 1607; c) K. Kim, C. Kim, Y. Byun, *Langmuir* **2001**, *17*, 5066 – 5070.
[20] M. Jurak, *Chem. Phys. Lipids* **2012**, *165*, 302 – 310.
[21] C. Huang, J. Mason, I. Levin, *Biochemistry* **1983**, *22*, 2775 – 2780.
[22] B. Voigtländer, in *Scanning probe microscopy*, Springer, Heidelberg, **2015**, pp. 115 – 121.
[23] C. Chen, N. Hayazawa, S. Kawata, *Nat. Commun.* **2014**, *5*, 3312.
[24] a) C. Lee, C. D. Bain, *Biochim. Biophys. Acta Biomembr.* **2005**, *1711*, 59 – 71; b) R. G. Snyder, H. L. Strauss, C. A. Elliger, *J. Phys. Chem.* **1982**, *86*, 5145 – 5150.
[25] a) C. J. Orendorff, M. W. Ducey, J. E. Pemberton, *J. Phys. Chem. A* **2002**, *106*, 6991 – 6998; b) C. B. Fox, R. H. Uibel, J. M. Harris, *J. Phys. Chem. B* **2007**, *111*, 11428 – 11436.

Manuscript received: May 6, 2021
Revised manuscript received: June 20, 2021
Accepted manuscript online: June 25, 2021
Version of record online: July 24, 2021

